SUPPLEMENTARY INFORMATION

A Hydrazone-Based Fluorescent Chemosensor for Al^{3+}: Turn-On Response Induced by ESIPT Suppression

Muzzaffar A. Bhat,*[a] Tabasum jan,[a] Refat Ashraf,[a] Muneeba Ali,[a] Asmat Mushtaq,[a] Sajad A Bhat,[a] Ray J. Butcher,[b] Noor U Din Reshi,*[a]
Department of Chemistry, Islamic University of Science and Technology Kashmir, 1-University Avenue. Awantipora-192122, Jammu and Kashmir, India
[b]Department of Chemistry, Howard University, Washington DC, 20059, USA.

Email: Muzzaffarbhat9@gmail.com (MAB)

Email: noor@iust.ac.in (NDR) https://orcid.org/0000-0001-9452-2608

24 Pages Including the Front Page

TABLE OF CONTENTS

General Comments:

Deuterated methanol (≥99%) with isotopic purity (99.9 atom% D), tert-butyl carbazate, and 2-hydroxy-1-naphthaldehyde were procured from Sigma Aldrich Chemicals India and were used without further purification. UV-vis and fluorescence experiments were carried out at room

temperature. UV-vis and fluorescence titration studies were conducted using 10 µM solutions of **KH** in MeOH. The solution of nitrates of Al^{3+}, Ca^{2+}, Cd^{2+}, Co^{2+}, Cu^{2+}, K^{+}, Mg^{2+}, Ni^{2+}, Zn^{2+}, Na^{+} and Fe^{3+} were prepared in methanol. The concentration of the metal ion solutions was 10 µM in both UV-vis and fluorescence experiments. A quartz cell with a 1 cm optical path length was used for each titration. The measurements of fluorescence emissions were taken 10 minutes after adding an aliquot of metal solution at λ_{ex} = 390 nm, using a 5.0 nm slit width for excitation and emission. The ^{1}H NMR and ^{13}C NMR spectra were recorded at 400 and 100 MHz respectively on a Bruker Spectrospin DPX–400 NMR spectrometer. TMS was used as an internal reference for NMR experiments.

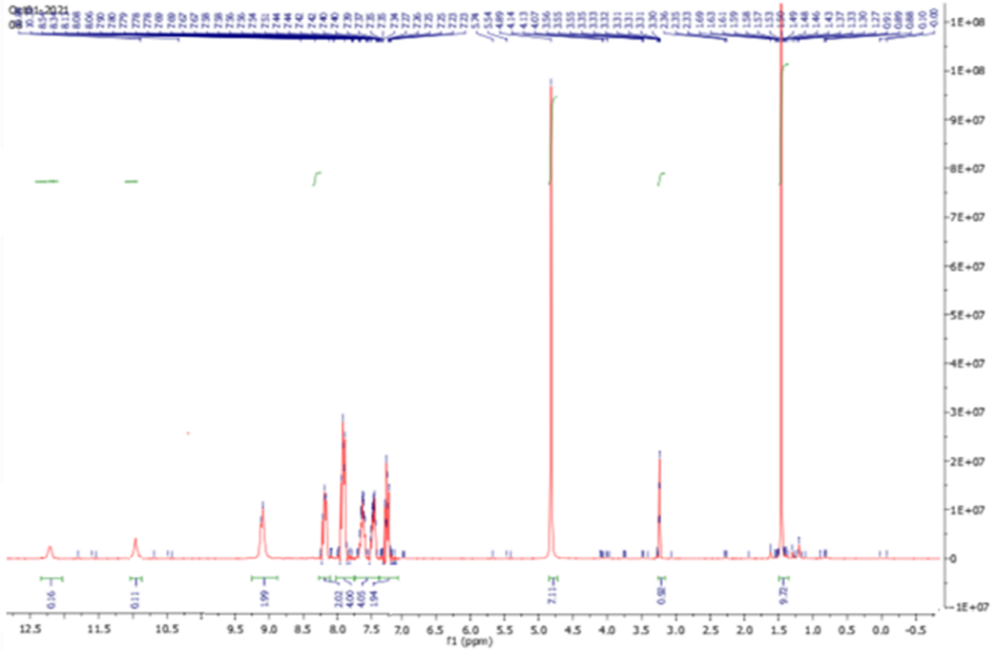

Fig S1. ^{1}H NMR spectrum of **KH**.

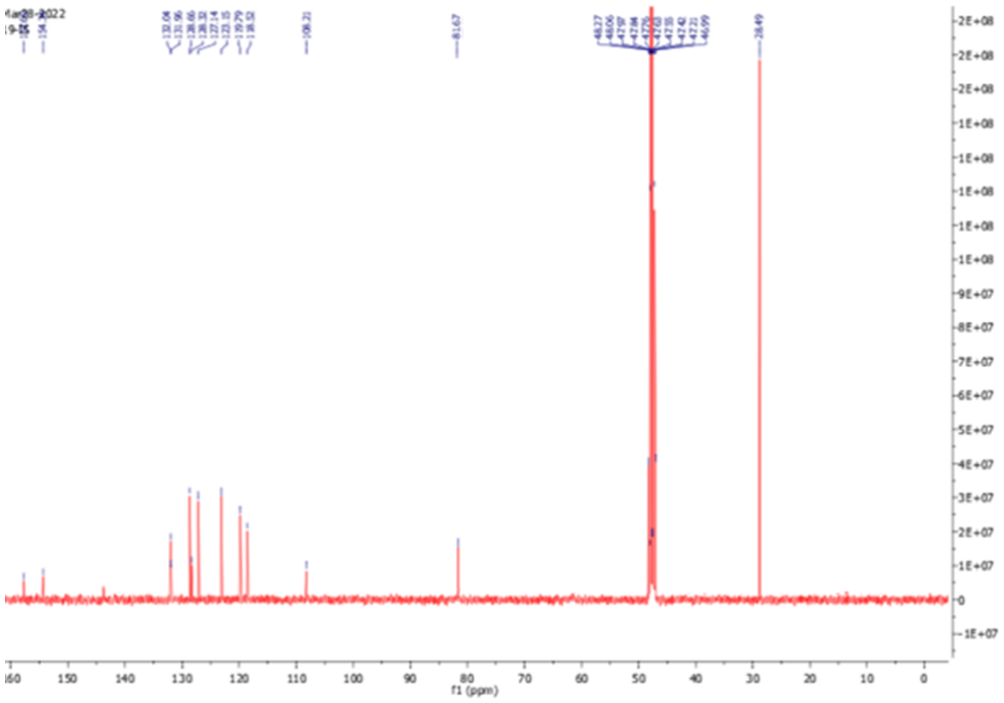

Fig S2. ^{13}C NMR spectrum of **KH**.

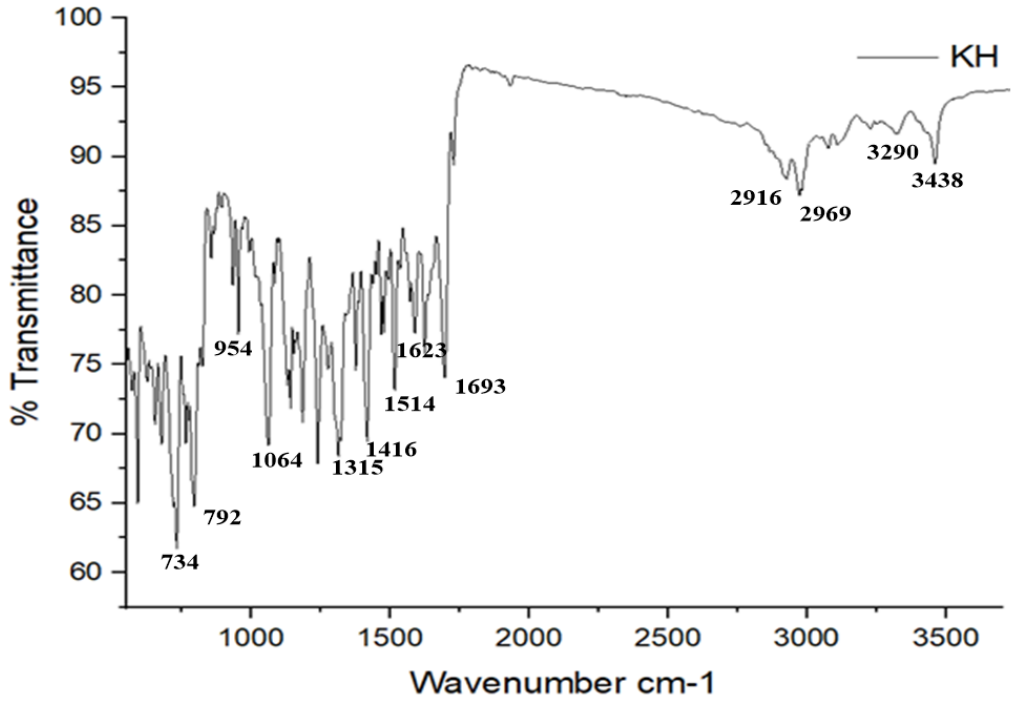

Fig S3. IR spectrum of **KH**.

Crystal data and structure refinement

Compound **KH** gave yellowish prismatic crystals upon recrystallisation from methanol. Mo-Kα (0.71073 Å) radiations at 100(2) were used to get the diffraction data of single crystals using a Bruker AXS SMART Apex CCD diffractometer. For absorption correction, SADABS was utilised, whereas software SHELXTL was employed for space group, structural determination, and refinements.[1] [2] Table S1 presents a summary of the crystal data and structural refinement results. The structural data is available in Cambridge Crystallographic Data Centre (CCDC 2380936). All the non-hydrogen atoms were refined in an anisotropic manner, and the hydrogen atoms (H's) were arranged in perfect locations with isotropic thermal characteristics by taking advantage of the hybridisation of the carbon. Different Fourier areas contained the hydrogen atoms.

Table S1. Crystal refinement parameters of compound **KH**.

	Compound KH **CCDC No. 2380936**
Empirical formula	C_{16} H_{18} N_2 O_3
Formula weight	286.32
Temperature	100(2) K
Wavelength	0.71073 Å
Crystal system	Monoclinic
Space group	P21/c
Unit cell dimensions	a = 12.5814(4) Å b = 11.6665(3) Å β= 102.112(2)°. c = 10.1069(3) Å
Volume	1450.48(7) Å^3

Z	4
Density(calculated)	1.311 Mg/m^3
Absorption coefficient	0.092 mm^{-1}
F(000)	608
Theta range for data collection	2.406 to 30.575°.
Index ranges	-17<=h<=17, -16<=k<=16, -14<=l<=14
Reflections collected	31402
Independent reflections	4452 [R(int) = 0.0775]
Completeness to theta = 25.242°	100 %
Refinement method	Full-matrix least-squares on F2
Data / restraints / parameters	4452/ 0 / 202
Goodness-of-fit on F2	1.034
Final R indices [I>2sigma(I)]	R1 = 0.0439, wR2 = 0.1096
R indices (all data)	R1 = 0.0603, wR2 = 0.1211
Extinction coefficient	0.017(3)
Largest diff. peak and hole	0.367 and -0.630 e.$Å^{-3}$

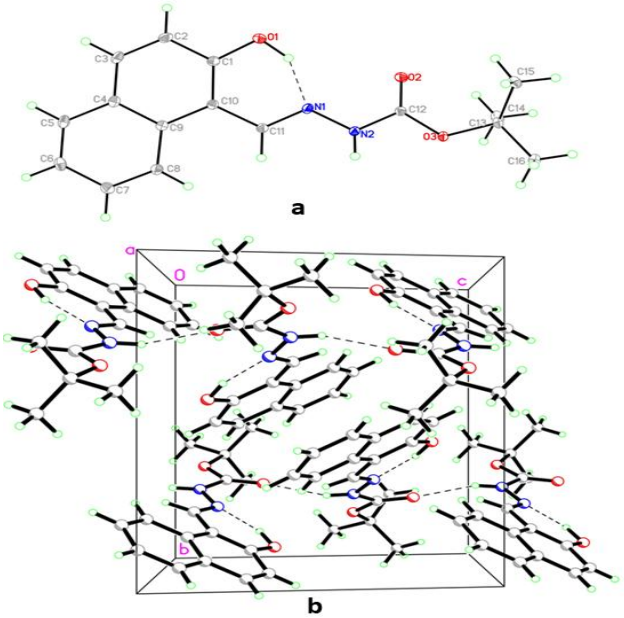

Fig. S4. (a) ORTEP diagram of **KH** with anisotropic displacement ellipsoids shown at the 50% probability level (b) the unit cell diagram seen along the b axis.

The asymmetric unit consists of the tert-butyl carbazate moiety (atoms N1–N2, O2–O3, C12–C16), a hydroxyl group (O1–H), and a naphthalene ring system (C1–C10). The centroids of the two aromatic

rings, designated as Cg1 and Cg2, correspond to ring systems C1–C5 and C6–C10, respectively. The structure reveals an intramolecular hydrogen bond between the hydroxyl hydrogen (O1–H) and the imine nitrogen (N1), with a short contact distance of 1.68(2) Å. This interaction, highlighted in Fig. S5 (pink), plays a stabilizing role in the molecular conformation. In addition, the carbonyl oxygen (O2), represented in green, forms a hydrogen bond with the adjacent hydrazine (N–H) proton, with a contact distance of 2.12(2) Å. A distinctive feature of the crystal packing is the formation of a carboxylic acid-type dimer, where the hydroxyl group of one molecule forms a hydrogen bond with the naphthyl hydrogen of a neighboring molecule. This reciprocal interaction results in the formation of an $R_2^2(8)$ ring motif, generating a stable eight-membered ring, with an interatomic separation of 2.49(2) Å, shown in blue in Fig. S5b. These non-covalent interactions particularly intramolecular hydrogen bonding and intermolecular dimerization contribute significantly to the stability and packing of the crystal lattice.

The overall stability of the supramolecular architecture is reinforced by both π…π and CH…π stacking interactions. In the studied compound, a similar non-covalent interaction is observed, where the centroid of the naphthalene ring (Cg2) forms a CH…π contact with a hydrogen atom from the methyl group of the tert-butyl substituent (C15H15B), with a distance of 3.380 Å, marked in orange (Fig. S5c). Additionally, the centroid of another naphthalene ring (Cg1) engages in a C–H…π interaction with a hydrogen atom located on a separate naphthalene unit (C7H7A), with an intermolecular distance of 3.023 Å, highlighted in magenta. Furthermore, Fig. S5c illustrates π–π stacking between two naphthalene rings, where the green lines represent centroid-to-centroid distances involving Cg1 and Cg2 from one aromatic system, and Cg3 and Cg4 from the interacting counterpart.

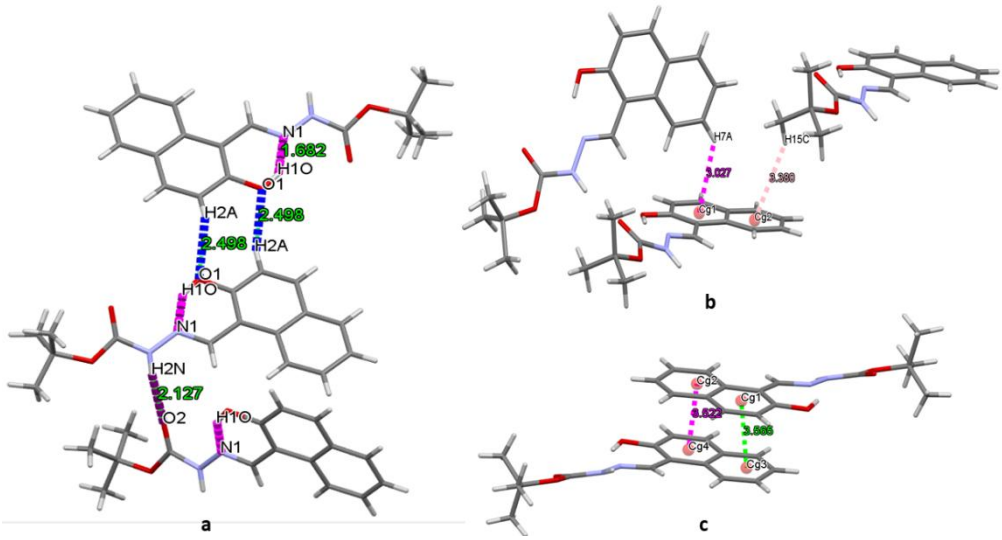

Fig S5. (a) Hydrogen bonding interactions. (b) Aromatic CH…Cg1 π, alkyl CH…Cg2 π interactions. (c) π…π stacking interactions.

Crystal structure related parameters.

Table S2. Atomic coordinates (x 104) and equivalent isotropic displacement parameters (Å2 x 103) for **KH**. U(eq) is defined as one third of the trace of the orthogonalized Uij tensor.

	x	Y	z	U(eq)
O(1)	6296(1)	4295(1)	1572(1)	23(1)
O(2)	8718(1)	2226(1)	2017(1)	20(1)
O(3)	9785(1)	1631(1)	4014(1)	18(1)

N(1)	7257(1)	2949(1)	3410(1)	15(1)
N(2)	8191(1)	2391(1)	4035(1)	17(1)
C(1)	5477(1)	4315(1)	2254(1)	18(1)
C(2)	4570(1)	4998(1)	1681(1)	22(1)
C(3)	3710(1)	5070(1)	2297(1)	21(1)
C(4)	3697(1)	4472(1)	3511(1)	17(1)
C(5)	2810(1)	4576(1)	4161(1)	20(1)
C(6)	2793(1)	4000(1)	5330(1)	23(1)
C(7)	3669(1)	3281(1)	5895(1)	23(1)
C(8)	4548(1)	3170(1)	5295(1)	19(1)
C(9)	4600(1)	3771(1)	4095(1)	15(1)
C(10)	5515(1)	3707(1)	3449(1)	15(1)
C(11)	6490(1)	3072(1)	4066(1)	15(1)
C(12)	8901(1)	2097(1)	3238(1)	15(1)
C(13)	10699(1)	1224(1)	3413(1)	17(1)
C(14)	10327(1)	219(1)	2478(1)	25(1)
C(15)	11133(1)	2215(1)	2705(1)	22(1)
C(16)	11527(1)	845(1)	4652(1)	24(1)

Table S3. Bond lengths [Å] and angles [°] for **KH**.

O(1)-C(1)	1.3552(13)
O(1)-H(1O)	0.95(2)
O(2)-C(12)	1.2161(13)
O(3)-C(12)	1.3354(12)
O(3)-C(13)	1.4859(12)
N(1)-C(11)	1.2893(13)
N(1)-N(2)	1.3757(12)
N(2)-C(12)	1.3658(13)
N(2)-H(2N)	0.883(15)
C(1)-C(10)	1.3930(15)
C(1)-C(2)	1.4120(15)
C(2)-C(3)	1.3595(16)
C(2)-H(2A)	0.95
C(3)-C(4)	1.4152(16)
C(3)-H(3A)	0.95
C(4)-C(5)	1.4144(15)
C(4)-C(9)	1.4235(14)
C(5)-C(6)	1.3629(17)
C(5)-H(5A)	0.95
C(6)-C(7)	1.4071(17)
C(6)-H(6A)	0.95
C(7)-C(8)	1.3740(15)
C(7)-H(7A)	0.95

C(8)-C(9)	1.4147(15)
C(8)-H(8A)	0.95
C(9)-C(10)	1.4392(14)
C(10)-C(11)	1.4564(14)
C(11)-H(11A)	0.95
C(13)-C(14)	1.5165(16)
C(13)-C(16)	1.5180(16)
C(13)-C(15)	1.5193(15)
C(14)-H(14A)	0.98
C(14)-H(14B)	0.98
C(14)-H(14C)	0.98
C(15)-H(15A)	0.98
C(15)-H(15B)	0.98
C(15)-H(15C)	0.98
C(16)-H(16A)	0.98
C(16)-H(16B)	0.98
C(16)-H(16C)	0.98
C(1)-O(1)-H(1O)	107.2(11)
C(12)-O(3)-C(13)	120.68(8)
C(11)-N(1)-N(2)	118.43(9)
C(12)-N(2)-N(1)	116.69(9)
C(12)-N(2)-H(2N)	121.8(9)
N(1)-N(2)-H(2N)	120.7(9)
O(1)-C(1)-C(10)	122.73(9)
O(1)-C(1)-C(2)	115.89(10)
C(10)-C(1)-C(2)	121.37(10)
C(3)-C(2)-C(1)	119.98(11)
C(3)-C(2)-H(2A)	120
C(1)-C(2)-H(2A)	120
C(2)-C(3)-C(4)	121.42(10)
C(2)-C(3)-H(3A)	119.3
C(4)-C(3)-H(3A)	119.3
C(5)-C(4)-C(3)	120.95(10)
C(5)-C(4)-C(9)	119.74(10)
C(3)-C(4)-C(9)	119.29(10)
C(6)-C(5)-C(4)	121.14(10)
C(6)-C(5)-H(5A)	119.4
C(4)-C(5)-H(5A)	119.4
C(5)-C(6)-C(7)	119.53(10)
C(5)-C(6)-H(6A)	120.2
C(7)-C(6)-H(6A)	120.2
C(8)-C(7)-C(6)	120.72(11)
C(8)-C(7)-H(7A)	119.6

C(6)-C(7)-H(7A)	119.6
C(7)-C(8)-C(9)	121.23(10)
C(7)-C(8)-H(8A)	119.4
C(9)-C(8)-H(8A)	119.4
C(8)-C(9)-C(4)	117.59(9)
C(8)-C(9)-C(10)	123.28(9)
C(4)-C(9)-C(10)	119.13(10)
C(1)-C(10)-C(9)	118.78(9)
C(1)-C(10)-C(11)	120.21(9)
C(9)-C(10)-C(11)	120.92(9)
N(1)-C(11)-C(10)	119.36(9)
N(1)-C(11)-H(11A)	120.3
C(10)-C(11)-H(11A)	120.3
O(2)-C(12)-O(3)	127.12(9)
O(2)-C(12)-N(2)	124.00(10)
O(3)-C(12)-N(2)	108.85(9)
O(3)-C(13)-C(14)	109.73(8)
O(3)-C(13)-C(16)	102.20(8)
C(14)-C(13)-C(16)	110.93(10)
O(3)-C(13)-C(15)	109.60(8)
C(14)-C(13)-C(15)	112.90(10)
C(16)-C(13)-C(15)	110.95(9)
C(13)-C(14)-H(14A)	109.5
C(13)-C(14)-H(14B)	109.5
H(14A)-C(14)-H(14B)	109.5
C(13)-C(14)-H(14C)	109.5
H(14A)-C(14)-H(14C)	109.5
H(14B)-C(14)-H(14C)	109.5
C(13)-C(15)-H(15A)	109.5
C(13)-C(15)-H(15B)	109.5
H(15A)-C(15)-H(15B)	109.5
C(13)-C(15)-H(15C)	109.5
H(15A)-C(15)-H(15C)	109.5
H(15B)-C(15)-H(15C)	109.5
C(13)-C(16)-H(16A)	109.5
C(13)-C(16)-H(16B)	109.5
H(16A)-C(16)-H(16B)	109.5
C(13)-C(16)-H(16C)	109.5
H(16A)-C(16)-H(16C)	109.5
H(16B)-C(16)-H(16C)	109.5

Table S4. Anisotropic displacement parameters (Å2 x 103) for **KH**. The anisotropic displacement factor exponent takes the form: -2p2[h2a*2U11 + ... + 2 h k a* b* U12].

	U11	U22	U33	U23	U13	U12
O(1)	22(1)	32(1)	16(1)	6(1)	6(1)	6(1)
O(2)	19(1)	26(1)	14(1)	0(1)	4(1)	1(1)
O(3)	13(1)	24(1)	16(1)	2(1)	4(1)	5(1)
N(1)	13(1)	17(1)	15(1)	0(1)	1(1)	3(1)
N(2)	14(1)	24(1)	12(1)	1(1)	2(1)	5(1)
C(1)	18(1)	20(1)	15(1)	-1(1)	3(1)	1(1)
C(2)	24(1)	25(1)	16(1)	4(1)	0(1)	6(1)
C(3)	18(1)	22(1)	21(1)	0(1)	-2(1)	6(1)
C(4)	14(1)	17(1)	19(1)	-4(1)	0(1)	0(1)
C(5)	13(1)	20(1)	27(1)	-5(1)	1(1)	2(1)
C(6)	16(1)	25(1)	30(1)	-4(1)	8(1)	-1(1)
C(7)	20(1)	26(1)	26(1)	2(1)	9(1)	-1(1)
C(8)	17(1)	20(1)	22(1)	3(1)	5(1)	2(1)
C(9)	14(1)	14(1)	16(1)	-2(1)	2(1)	-1(1)
C(10)	14(1)	15(1)	15(1)	-1(1)	2(1)	1(1)
C(11)	15(1)	16(1)	14(1)	0(1)	2(1)	0(1)
C(12)	14(1)	16(1)	15(1)	0(1)	3(1)	0(1)
C(13)	14(1)	19(1)	21(1)	-1(1)	7(1)	2(1)
C(14)	22(1)	21(1)	35(1)	-8(1)	10(1)	-2(1)
C(15)	19(1)	23(1)	25(1)	0(1)	8(1)	-3(1)
C(16)	17(1)	30(1)	25(1)	4(1)	5(1)	6(1)

Table S5. Hydrogen coordinates (x 10^4) and isotropic displacement parameters (Å2 x 10^3) for **KH**.

	x	y	z	U(eq)
H(1O)	6840(16)	3793(17)	2050(20)	51(5)
H(2N)	8370(11)	2340(12)	4926(15)	20(3)
H(2A)	4562	5407	866	27
H(3A)	3104	5533	1903	25
H(5A)	2216	5057	3778	24
H(6A)	2195	4082	5759	27
H(7A)	3653	2867	6700	28
H(8A)	5131	2681	5694	23
H(11A)	6560	2752	4944	18
H(14A)	9983	-356	2957	38
H(14B)	10956	-122	2195	38
H(14C)	9803	486	1680	38
H(15A)	10642	2359	1832	32
H(15B)	11857	2020	2557	32
H(15C)	11181	2903	3270	32

H(16A)	11211	244	5127	36
H(16B)	11732	1501	5258	36
H(16C)	12174	546	4372	36

Table S6. Torsion angles [°] for **KH**.

C(11)-N(1)-N(2)-C(12)	168.74(9)
O(1)-C(1)-C(2)-C(3)	-179.94(10)
C(10)-C(1)-C(2)-C(3)	-0.15(18)
C(1)-C(2)-C(3)-C(4)	-0.03(18)
C(2)-C(3)-C(4)-C(5)	178.34(11)
C(2)-C(3)-C(4)-C(9)	-0.51(17)
C(3)-C(4)-C(5)-C(6)	179.88(11)
C(9)-C(4)-C(5)-C(6)	-1.27(16)
C(4)-C(5)-C(6)-C(7)	-0.45(17)
C(5)-C(6)-C(7)-C(8)	1.15(18)
C(6)-C(7)-C(8)-C(9)	-0.09(18)
C(7)-C(8)-C(9)-C(4)	-1.60(16)
C(7)-C(8)-C(9)-C(10)	178.32(10)
C(5)-C(4)-C(9)-C(8)	2.26(15)
C(3)-C(4)-C(9)-C(8)	-178.88(10)
C(5)-C(4)-C(9)-C(10)	-177.66(9)
C(3)-C(4)-C(9)-C(10)	1.20(15)
O(1)-C(1)-C(10)-C(9)	-179.38(10)
C(2)-C(1)-C(10)-C(9)	0.84(16)
O(1)-C(1)-C(10)-C(11)	3.99(16)
C(2)-C(1)-C(10)-C(11)	-175.79(10)
C(8)-C(9)-C(10)-C(1)	178.72(10)
C(4)-C(9)-C(10)-C(1)	-1.36(15)
C(8)-C(9)-C(10)-C(11)	-4.67(16)
C(4)-C(9)-C(10)-C(11)	175.24(9)
N(2)-N(1)-C(11)-C(10)	177.14(9)
C(1)-C(10)-C(11)-N(1)	-9.29(15)
C(9)-C(10)-C(11)-N(1)	174.16(10)
C(13)-O(3)-C(12)-O(2)	1.61(16)
C(13)-O(3)-C(12)-N(2)	179.79(8)
N(1)-N(2)-C(12)-O(2)	-5.50(16)
N(1)-N(2)-C(12)-O(3)	176.24(8)
C(12)-O(3)-C(13)-C(14)	-65.73(12)
C(12)-O(3)-C(13)-C(16)	176.51(9)
C(12)-O(3)-C(13)-C(15)	58.78(12)

Symmetry transformations used to generate equivalent atoms:

Table S7. Hydrogen bonds for **KH** [Å and °].

D-H...A	d(D-H)	d(H...A)	d(D...A)	<(DHA)
O(1)-H(1O)...N(1)	0.95(2)	1.68(2)	2.5366(12)	147.3(17)
N(2)-H(2N)...O(2)#1	0.883(15)	2.128(15)	2.9809(12)	162.2(13)
C(2)-H(2A)...O(1)#2	0.95	2.5	3.3427(14)	148.1
C(14)-H(14C)...O(2)	0.98	2.51	3.0659(14)	115.9
C(15)-H(15A)...O(2)	0.98	2.47	2.9720(14)	111.4

Symmetry transformations used to generate equivalent atoms: #1 x,-y+1/2,z+1/2 #2 -x+1,-y+1,-z

Hirshfeld surface calculations:

The utilisation of Hirshfeld surfaces [3] and the related two-dimensional fingerprint plots [4] can aid in the examination of intermolecular interactions in an extensive array of organic and inorganic substances. Hirshfeld surface features (dnorm, shape index, or curvedness) are characterised by different functions, which enable visual analysis and intuitive recognition of interactions between different molecules [6].[5] Because red patches on the norm surface are associated with atom-to-atom connections shorter than the sum of the van der Waals (vdW) radii, they are frequently used to depict intimate interactions, such as hydrogen bonds. The two-dimensional fingerprint plots provide a graphical depiction of the contact distances to the Hirshfeld surface and allow us to interpret and measure the intermolecular interactions within the crystal lattice. Two-dimensional fingerprint plots and Hirshfeld surfaces were examined using the CrystalExplorer17.5 application by importing crystal structure from CIF files.[6]

The three-dimensional Hirshfeld surface (HS) analysis of **KH** was performed to investigate the nature and contributions of intermolecular interactions within the crystal lattice. The dnorm-mapped HS displays a range from –1.2398 to +1.4008 Å, effectively highlighting regions of close contact and potential hydrogen bonding.

To further quantify and differentiate the types of interactions, two-dimensional fingerprint plots (2D-FPs) were generated by plotting the internal (di) versus external (de) distances from the surface. These fingerprint plots provide a unique “interaction signature” for each molecule, allowing the visualization of individual contributions to crystal packing.

The dnorm-mapped surface for compound KH (Fig. S6a and S6b) shows distinct red regions, indicating close contacts such as N–H···O, C–H···O, and O–H···N hydrogen bonds, along with weaker contacts involving C–C, C–H, and H–H interactions. These red spots are consistent with moderate hydrogen bonds and van der Waals interactions that collectively stabilize the crystal structure. Notably, H···H interactions, with di + de < 2.4 Å, make the largest contribution to molecular packing. Although these contacts are only marginally shorter than the sum of the van der Waals radii, they play a significant role in maintaining crystal cohesion. [7]

The HS was visualized from two orientations by rotating the molecule 180° along the horizontal axis (Fig. S6a and S6b). In both orientations, red regions labeled 1 correspond to strong reciprocal O–H···O and N–H···O hydrogen bonds, specifically between the carbonyl oxygen and hydrazine

hydrogen. Red patches labeled 2 reflect reciprocal O···H/H···O interactions between the hydroxyl oxygen and the naphthyl hydrogen. Additionally, the region marked 3 represents a C–H···π interaction, while label 4 denotes π···π stacking between aromatic systems.

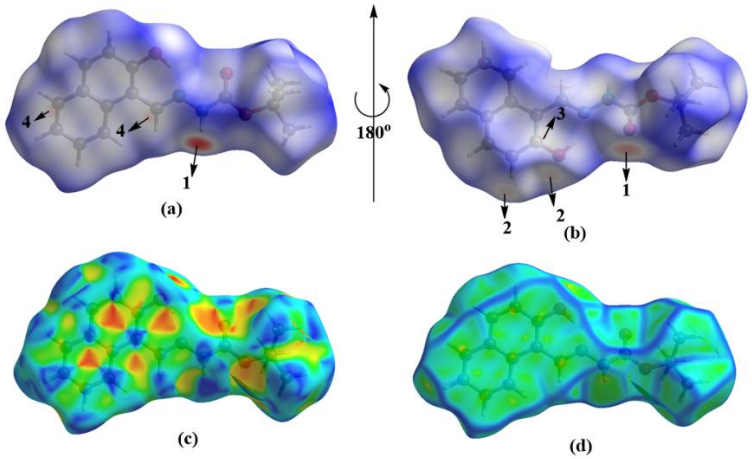

Fig. S6. (a) and (b) Mapped using dnorm are the Hirshfeld surfaces of **KH** in two orientations. (c) Hirshfeld surfaces of **KH** that have been mapped using shape index and (d) curvedness values.

Quantitative analysis of the HS reveals that: H···H interactions contribute 52.1% of the total surface area, H···C/C···H contacts account for 20.6%, H···O/O···H interactions represent 16.5%, while C···C and H···N/N···H interactions contribute 5.9% and 4.9%, respectively. There is negligible contribution from O···C contacts, suggesting that such interactions do not play a significant role in the crystal packing of **KH**.

Given the presence of extended π-systems, π···π stacking interactions were further examined using the Shape Index and Curvedness features of the Hirshfeld surface. [8] As shown in Fig. S6c, red and blue "bow-tie" patterns on the shape index map are indicative of face-to-face π-stacking, particularly involving the naphthalene moiety. This characteristic pattern confirms the planar stacking of six-membered aromatic rings in the structure. [9] Complementing this, the curvedness map (Fig. S6d) displays large green flat regions, further supporting the existence of extensive π···π interactions contributing to the supramolecular framework.

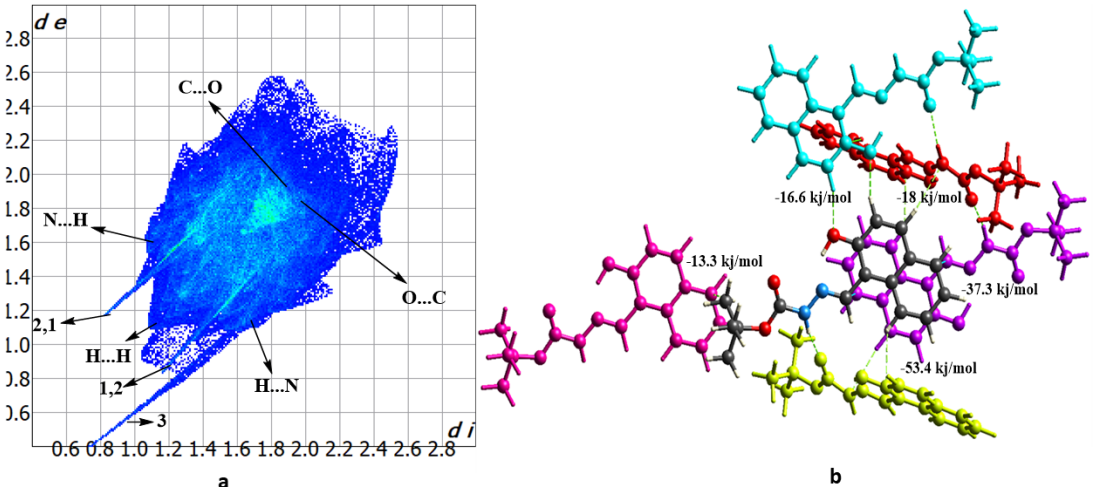

Fig. S7. (a) 2D fingerprint plot showing various contacts. (b) Molecular pairs with their interaction energies for **KH**.

The comprehensive 2D fingerprint plot (Fig. S7a) summarizes the dominant intermolecular interactions. The most intense region of the plot (marked at de + di ≈ 2.4 Å) corresponds to H···H contacts, underscoring their role in molecular cohesion. Labels 1 and 2 on the plot denote the characteristic interaction patterns observed on the Hirshfeld surface.

Energy Frameworks:

To gain a deeper understanding of the intermolecular interactions governing crystal packing, the energy frameworks of **KH** were calculated using the Crystal Explorer 17.5 software, employing the B3LYP/6-311G(d,p) level of theory. This approach enables quantitative assessment of interaction energies between molecular pairs within the crystal lattice, providing insight into the forces responsible for supramolecular assembly.

The total interaction energy (Etot) between two molecules is obtained by summing four key energy components: Electrostatic (E_ele), Polarization (E_pol), Dispersion (E_dis), Exchange-repulsion (E_rep)

These components are scaled by default factors in CrystalExplorer: Electrostatics (E_ele): 0.618, Polarization (E_pol): 0.740, Dispersion (E_dis): 0.871, Repulsion (E_rep): 1.057.[10 11]

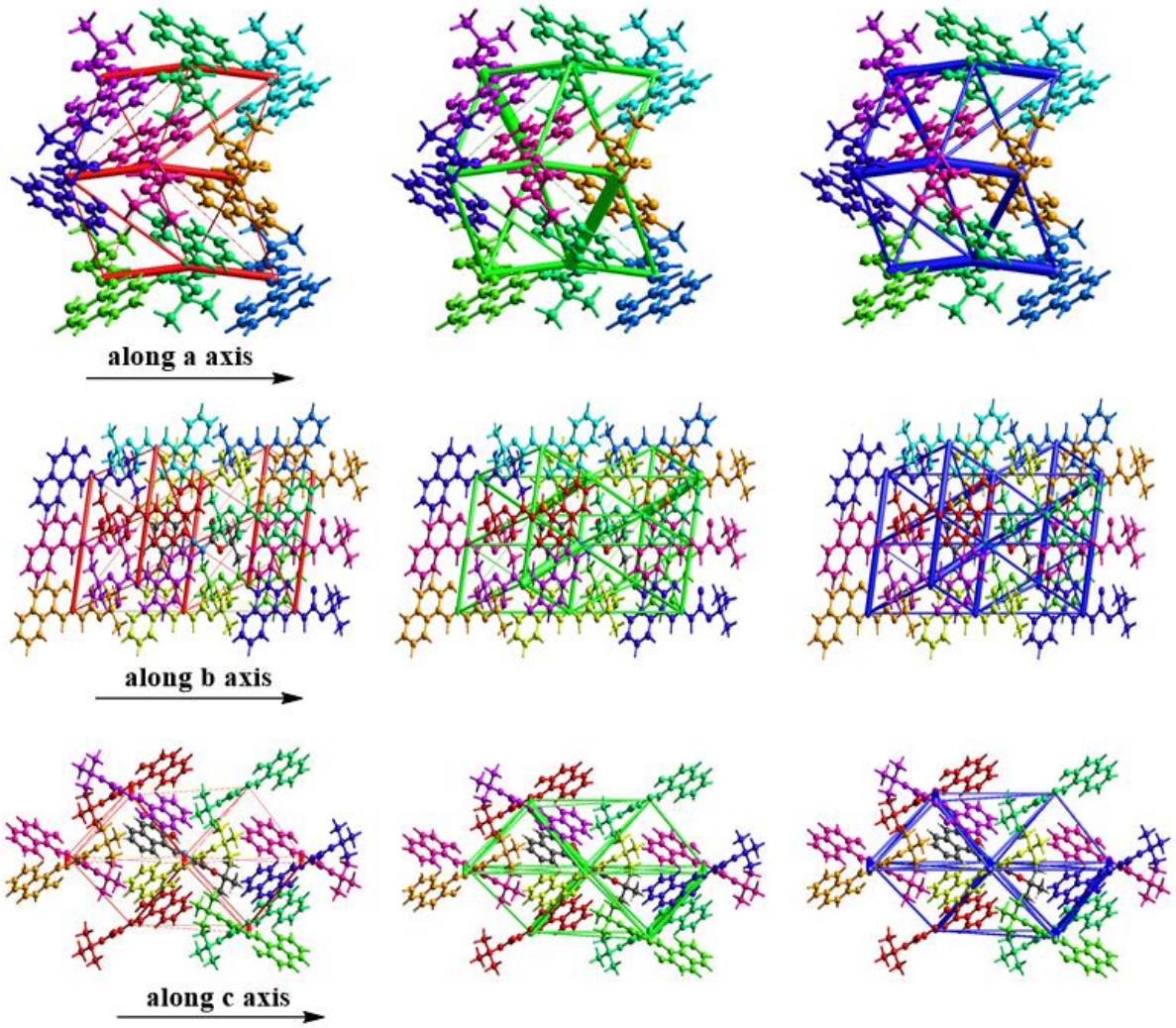

Fig. S8. Energy frameworks along the a-c axes for **KH**.

The calculated energy frameworks are visualized along the a–c crystallographic plane (Fig. S8), illustrating the spatial arrangement and relative strength of interactions. The cylinders connecting

molecular centroids represent the interaction energies, with their thickness proportional to energy magnitude. Detailed interaction energies for specific molecular pairs are presented in Table 8b.

One of the most significant contributions to the crystal packing arises from C–H···π interactions and N–H···O=C hydrogen bonds, exhibiting a total interaction energy of –53.4 kJ·mol^{-1}, as shown in Table 8a and Fig. S8b. A second key interaction involves dimer formation via reciprocal hydrogen bonding, with a relatively strong interaction energy of –16.6 kJ·mol^{-1}. Additionally, π···π stacking interactions between aromatic systems contribute to the lattice stabilization, with an associated interaction energy of –37.3 kJ·mol^{-1}. These findings are consistent with the geometrical features previously described in the single-crystal X-ray diffraction section.

The net energy framework analysis further reveals that the crystal structure is primarily stabilized by dispersion interactions, with a value of –228.5 kJ·mol^{-1}, followed by a significant electrostatic component of –72.6 kJ·mol^{-1}. This is reflected in the energy framework diagram (Fig. S8), where the thickest cylinders represent dispersion-dominated interactions along the a–c axis. The close correlation between structural geometry and energy calculations supports the robustness of the packing model.[12]

Table S8 (a). Displays the total lattice energies of **KH**, as a function of coulombic, polarization, dispersion, and repulsion. (b) The energy of interaction (Kcal/mol) between chemical pairs linked by symmetry operations and the crystal's interaction mapping.

(a) Compound	E_{coul}	E_{Pol}	E_{Disp}	E_{Rep}	E_{Tot}
1	-72.6	-20.8	-228.5	149.8	-196.6

(b) N[a]	Symmetry code	R[b]	E_{ele}	E_{pol}	E_{dis}	E_{rep}	E_{Tot}
2	-x, y+1/2, -z+1/2	11.38	-3.2	-2.0	-25.7	15.0	-18.0
2	x, -y+1/2, z+1/2	07.88	-2.4	-0.4	-11.7	0.0	-13.0
2	x, -y+1/2, z+1/2	12.12	-34.8	-7.7	-40.0	38.6	-53.4
1	-x, -y, -z	15.71	-2.9	-0.6	-22.8	12.6	-15.5
2	-x, y+1/2, -z+1/2	08.79	-6.3	-1.8	-16.7	8.2	-17.5
1	-x, -y, -z	05.81	-13.4	-3.9	-14.9	21.6	-16.6
1	-x, -y, -z	06.58	-2.1	-0.2	-2.2	0.0	-4.3
2	x, -y+1/2, z+1/2	09.19	0.0	-0.2	-8.6	0.0	-7.7
1	-x, -y, -z	08.71	-6.6	-3.4	-70.0	53.8	-37.3
2	x, y, z	08.69	-0.9	-0.6	-15.9	0.0	-13.3

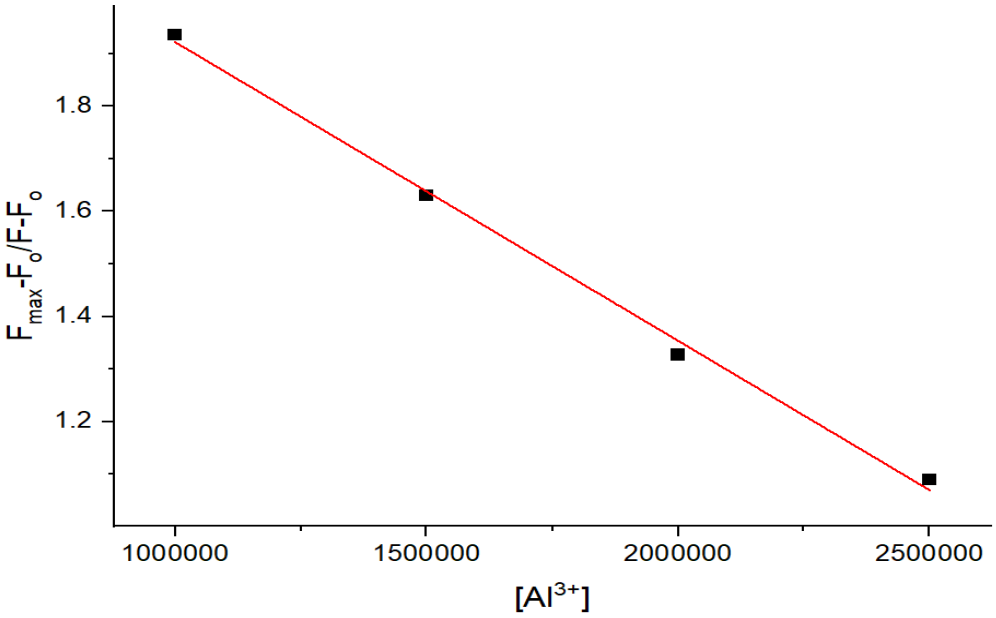

Fig. S9. Calculation of binding constant for Al^{3+} with **KH** from the plot $(A_F-A_o)/(A_X-A_o)$ Vs 1/ $[Al^{3+}]$.

Visual Detection of Al^{3+} Using KH-Coated TLC Strips.

TLC plate strips were coated with a methanolic solution of **KH** and dried under ambient conditions. Upon exposure to Al^{3+}-spiked water samples, the strips exhibited a light green coloration visible to the naked eye, whereas no noticeable color change was observed in the absence of Al^{3+}. The observed color change arises from the Al^{3+}-induced red shift in the absorption spectrum of **KH**, confirming the feasibility of rapid and visual detection of Al^{3+} in aqueous media.

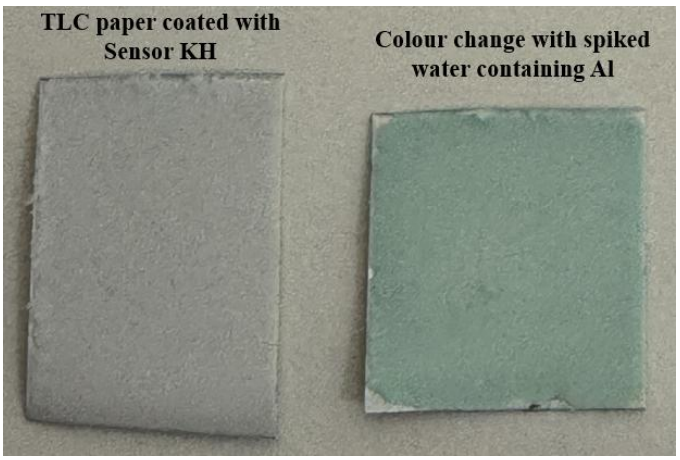

Fig. S10. Visual response of **KH**-coated TLC strips toward Al^{3+} in spiked water samples.

Al^{3+}/Zn^{2+} Competitive Binding

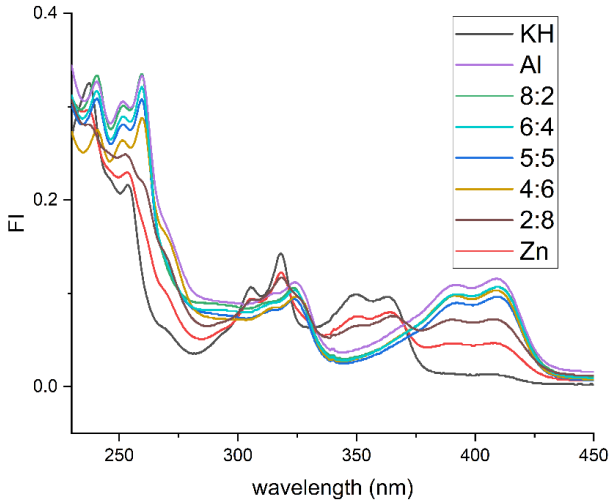

Fig. S11. Fluorescence intensity changes of **KH** in the presence of Zn^{2+} upon incremental addition of Al^{3+}.

Competitive binding experiments were carried out by varying the Al^{3+}:Zn^{2+} ratio while keeping the probe concentration constant. With increasing Al^{3+} content, the absorption spectrum progressively converged toward that of the **KH**–Al^{3+} complex, while the spectral features associated with Zn^{2+} diminished. Even in the presence of excess Zn^{2+}, Al^{3+} retained its characteristic absorption response, indicating a stronger binding affinity of **KH** toward Al^{3+} compared to Zn^{2+}. competitive binding experiments were carried out by varying the Al^{3+}:Zn^{2+} ratio while keeping the probe concentration constant. With increasing Al^{3+} content, the absorption spectrum progressively converged toward that of the **KH**–Al^{3+} complex, while the spectral features associated with Zn^{2+} diminished. Even in the presence of excess Zn^{2+}, Al^{3+} retained its characteristic absorption response, indicating a stronger binding affinity of **KH** toward Al^{3+} compared to Zn^{2+}.

Effect of pH.

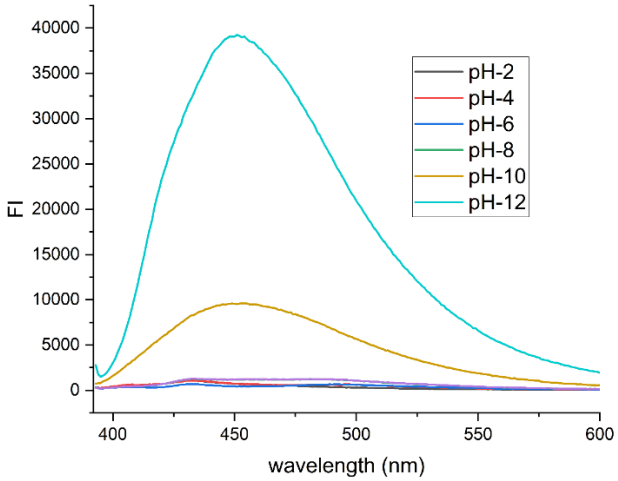

Fig. S12. pH-dependent fluorescence intensity of free **KH** measured over the pH range 2–12.

The free sensor **KH** exhibits negligible fluorescence from pH 2 to 8. A weak emission gradually appears at pH 10 and becomes slightly more pronounced at pH 12. This behavior can be attributed to deprotonation of the phenolic –OH group under strongly basic conditions, which perturbs the ESIPT equilibrium and partially suppresses non-radiative decay pathways. Importantly, this base-induced fluorescence is weak and occurs only under highly alkaline conditions; therefore, it does not interfere with the sensing performance of **KH** toward Al^{3+} in the neutral pH range. The probe remains operationally stable and essentially non-emissive in the relevant pH window (2–8).

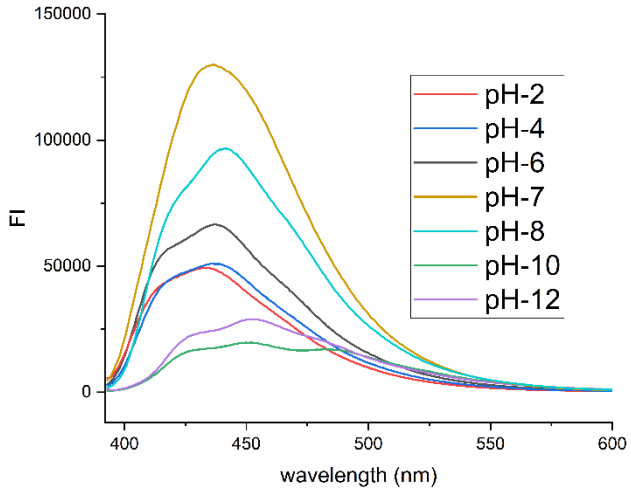

Fig. S13. pH-dependent fluorescence intensity of the **K**–Al^{3+} complex measured over the pH range 2–12.

For the **KH**–Al^{3+} system, a strong fluorescence enhancement is observed in the pH range 6–8, indicating optimal complex formation under near-neutral conditions. At pH 2 and 4, the fluorescence intensity remains appreciable, suggesting that coordination between **KH** and Al^{3+} is retained under mildly acidic conditions. In contrast, a pronounced decrease in fluorescence intensity is observed at pH 10 and 12, which can be attributed to hydroxide-induced hydrolysis of Al^{3+} and competitive binding by OH^- ions, leading to dissociation of the **KH**–Al^{3+} complex. These results demonstrate that **KH** exhibits optimal sensing performance toward Al^{3+} in the neutral pH region.

While methanol was used for titration experiments to achieve optimal solubility and consistent spectral responses, pH studies necessitate the use of water for effective proton activity and buffer action. Accordingly, a MeOH:H_2O (8:2, v/v) medium was used as the solvent. Pure methanol does not allow meaningful pH control; hence a small fraction of water was introduced only for pH studies without affecting the sensing mechanism

Table S9. Comparison of selected Al^{3+} fluorescence chemosensors with **KH**.

Entry	Probe	LOD	Reference
1	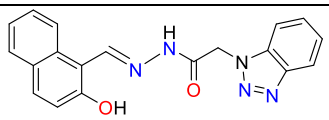 Tumay et al (2021)	3.4×10^{-7} M	[13]
2	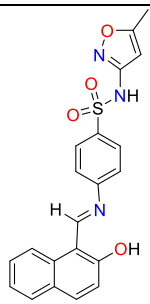 Sinha et al. (2015)	3.3×10^{-7} M	[14]
3	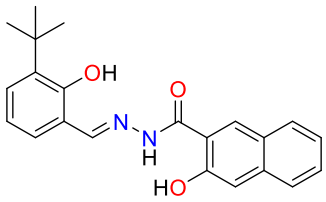 Choe and Kim (2021)	8.3×10^{-7} M	[15]
4	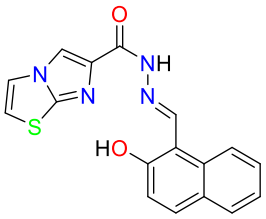 Zhang et al. (2019)	1.4×10^{-7} M	[16]
5	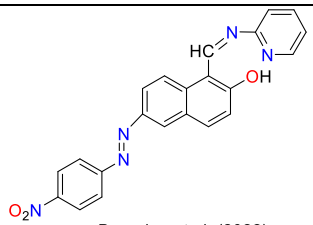 Banerjee et al. (2022)	5.4×10^{-7} M	[17]
6	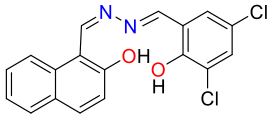 Anshori et al. (2022)	4.0×10^{-8} M	[18]

7	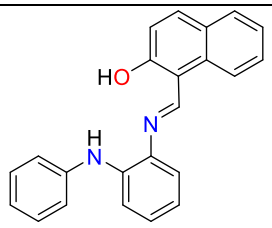 Vikraman et al. (2023)	2.4×10^{-8} M	[19]
8	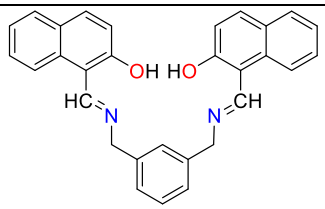 Nandhakumar et al. (2025)	8.8×10^{-9} M	[20]
9	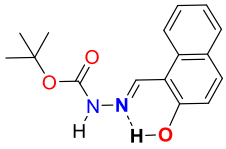 **KH**	3.6×10^{-7} M	This work

Fluorescence Quantum Yield.

ESIPT-active fluorophores typically exhibit very low fluorescence quantum yields due to ultrafast proton transfer and dominant non-radiative relaxation pathways. To verify the involvement of the ESIPT mechanism, relative fluorescence quantum yields were determined using Coumarin 535 as the reference standard. For quantum yield measurements, the absorbance at the excitation wavelength (λ_{ex}) for the reference dye Coumarin 535, free sensor **KH**, **KH** with 0.5 equivalents of Al^{3+}, and **KH** with 1.0 equivalent of Al^{3+} was carefully adjusted to 0.04, which lies within the acceptable absorbance range of 0.02–0.04 required for reliable quantum yield determination and to minimize inner filter effects. The free sensor **KH** displayed a very low quantum yield, consistent with an active ESIPT process. Upon coordination with Al^{3+}, a pronounced increase in the quantum yield was observed, indicating effective suppression of the ESIPT pathway through metal binding involving the phenolic oxygen and imine nitrogen atoms. The fluorescence quantum yield (Φ_x) was calculated using the following relation:

$\Phi_x = \Phi\_ref \times (I_x/I\_ref) \times (A\_ref/A_x) \times (n_x^2/n\_ref^2)$,

where Φ_ref is the quantum yield of the reference, I is the integrated emission intensity, A is the absorbance at the excitation wavelength, and n is the refractive index.

To ensure accurate determination of quantum yields, the absorbance of Coumarin 535, free **KH**, and the **KH**–Al^{3+} complex at the excitation wavelength was maintained below 0.05.

Table S10: Fluorescence quantum yields of **KH**, **KH** + 0.5 equiv. of Al^{3+} and **KH** + 1 equiv. of Al^{3+}

Coumarin 535	Sensor **KH**	**KH**+0.5 equiv. of Al	**KH**+1 equiv. of Al
Area (11295704)	Area (308278)	Area (1915553)	Area (3931525)
Φ=0.69	Φ=0.018	Φ=0.117	Φ=0.240

Using this approach, the free sensor **KH** exhibited a low quantum yield (Φ = 0.018). Upon addition of 0.5 equivalents of Al^{3+}, the quantum yield increased to Φ = 0.117 (≈6.5-fold enhancement), indicating partial suppression of the ESIPT process. Further addition of Al^{3+} to 1.0 equivalent resulted in a quantum yield of Φ = 0.240 (≈13-fold enhancement), consistent with more effective ESIPT blocking. These results clearly support that the fluorescence enhancement arises predominantly from coordination-induced suppression of ESIPT rather than CHEF or solvent effects.

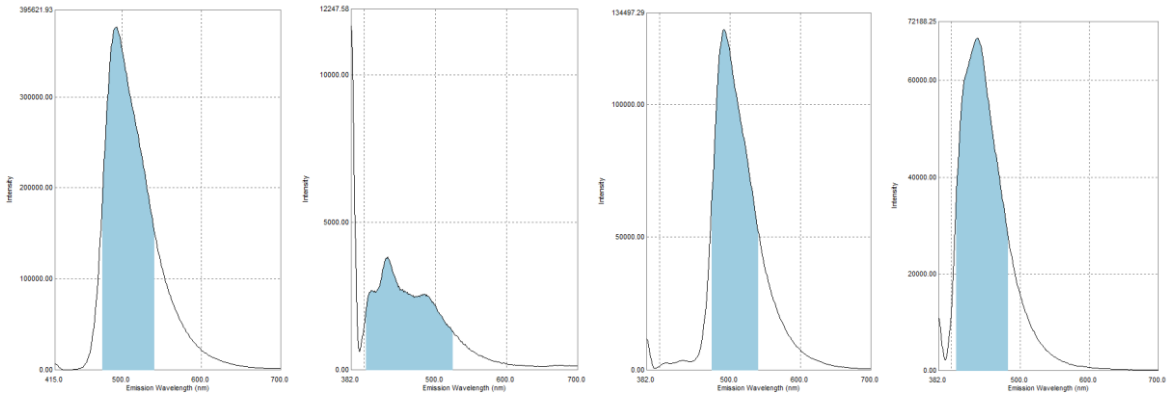

Fig. S14. Integrated area for ref, sensor **KH**, **KH** = 0.5 eq Al^{3+} and **KH** + 1 equiv. of Al^{3+}

DFT Calculations:

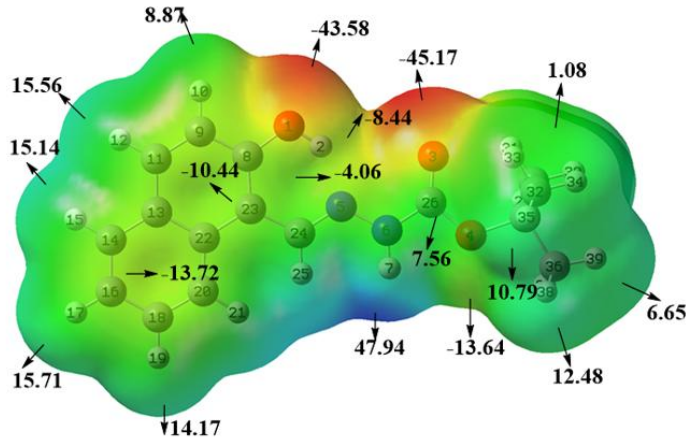

a

Fig. S15. ESP map of **KH**.

Table S11. Excitation energy, oscillator strength and major electronic configuration of **KH** in absorption and emission states.

Excited State	λ (nm) cal.	E (eV) cal.	f	Configuration
Absorption				
S1	318.52	3.8925	0.4777	76 →77 H → L

S2	276.80	4.4792	0.1583	75→ 77 H-1→L
S3	252.93	4.9020	0.0448	76 → 78 H →L+1
S4	228.68	5.4218	0.7524	76 → 79 H →L+2
S5	222.19	5.5800	0.3116	74 → 77 H-2 → L
S6	219.61	5.6457	0.0006	72 → 77 H-4 → L
S7	210.50	5.8899	0.3677	75 → 78 H-1 →L+1
S8	202.02	6.1372	0.2916	75→79 H-1 → L+2
S9	192.55	6.4391	0.0001	73 → 77 H-3 → L
S10	191.94	6.4594	0.2776	74 → 78 H-2 →L+1
Emission				
S1	388.69	3.1898	0.7259	76 → 77 H→L
S2	297.26	4.1709	0.2508	75 →77 H-1→L
S3	274.27	4.5206	0.0565	76→ 78 H→L+1
S4	249.00	4.9794	0.7589	76 → 79 H →L+2
S5	242.65	5.1096	0.5049	74→ 77 H-2 →L

Table S12. Excitation energy, oscillator strength and major electronic configuration of **Al–K** in absorption and emission states.

Excited State	λ (nm) cal.	E (eV) cal.	f	Configurations
Absorptions				
S1	374.83	3.3077	0.4476	81 →82 H → L
S2	333.25	3.7205	0.1141	80 →82 H-1 → L
S3	300.32	4.1284	0.0072	81 → 83 H → L+1
S4	259.84	4.7716	0.2624	79 → 82 H-2 → L
S5	252.94	4.9017	0.0013	80 → 83 H-1 → L+1
S6	241.56	5.1327	0.0648	80 → 84 H-1 → L+2
S7	239.25	5.1823	0.0922	81 → 84 H → L+2
S8	215.74	5.7469	0.0000	76 → 82 H-4 → L
S9	210.96	5.8772	0.9856	81 → 85 H → L+3
S10	204.31	6.0684	0.0021	79 → 83 H-2 → L+1
Emissions				
S1	439.55	2.8207	0.5793	81 → 82 H → L
S2	352.27	3.5196	0.1799	80 → 82 H-1 → L
S3	299.98	4.1331	0.0089	81 → 83 H → L+1
S4	279.38	4.4379	0.2802	79 → 82 H-2→L
S5	255.05	4.8611	0.1860	79 → 82 H-2→L

References

1 G. M. Sheldrick, *Crystallogr.* **64**, 112–122 (2008).

2. G. M. Sheldrick, *Acta Crystallogr. Sect. A Found. Adv.* **71**, 3–8 (2015).

3. J. J. McKinnon, M. A. Spackman and A. S. Mitchell, *Acta Cryst*. (2004). B60, 627-668.

4. J. J. McKinnon, D. Jayatilakaa and M. A. Spackmana, *Chem. Commun*., 2007, 3814-3816.

5. A. Saeed, U. Flörke, A. Fantoni, A. Khurshid, H. Pérez and Mauricio F. Erben, *CrystEngComm,* 2017,**19**, 1495-1508.

6. P. R. Spackman, M. J. Turner, J. J. McKinnon, S. K. Wolff, D. J. Grimwood, D. Jayatilak and M. A. Spackmanba, *J. Appl. Cryst., 2021,* 1006-1011.

7. S. K. Seth, *Acta Crystallogr. E: Cryst. Struct. Commun*.,2018, 74, 600-606.

8. M. A. Spackman, P. G. Byrom, *Chem. Phys. Lett*. 1997, 267, 215-220).

9. J. J. McKinnon, A. S. Mitchell, M. A. Spackman, *Chem. Eur. J.,* 1998, 4, 2136-2141.

10. C. Jelsch, S. Soudania and C. B. Nasrb, *IUCrJ*, 2015, 2, 327-340.

11. J. J. McKinnon, A. S. Mitchell and M. A. Spackman, *Chem. Commun*., 1998, 2071-2072.

12. A. Saeed, M. Bolte, M. F. Erben and H. Pérez, *CrystEngComm*, 2015, 17, 7551-7563.

13. S. O. Tümay, A. Şenocak and A. Mermer, *NJC*, 2021, **45**, 18400–18411.

14. S. Mondal, A. K. Bhanja, D. Ojha, T. K. Mondal, D. Chattopadhyay and C. Sinha, *RSC Adv*., 2015,**5**, 73626-73638.

15. D. Choe and C. Kim, *Mater.,* 2021, **14**, 6392.

16. Y. Xu, H. Wang, J. Zhao, X. Yang, M. Pei, G. Zhang and Y. Zhang, NJC, 2019, 43, 14320–14326.

17. S. Mabhai, M. Dolai, S. K. Dey, S. M. Choudhury, B. Das, S. Dey, A. Jana and D. R. Banerjee, *NJC,* 2022, **46**, 6885–6898.

18. J. Al Anshori, D. Ismalah, A. F. Abror, A. Zainuddin, I. Wiani Hidayat, M. Yusuf, R. Maharani and A. Tatang Hidayat, *RSC Adv.*, 2022, **12**, 2972–2979.

19. T. J. Dathees, S. P. M. Paul, A. Sanmugam, A. Abiram, S. Murugan, R. S. Kumar, A. I. Almansour, N. Arumugam, R. Nandhakumar and D. Vikraman, *Spectrochim Acta A Mol Biomol Spectrosc,* 2024, **308**, 123732.

20. E. Antony, N. Ganesan, K. Srinivasan, S. P. M. Paul, A. Abiram, K. Parvatham, V. R. Kannan and R. Nandhakumar, *NJC,* 2025, **49**, 14787–14800.